Anthracene-induced formation of highly twisted metallacycle and its crystal structure and tunable assembly behaviors

Chongyi Chen[a,1], Yan Sun[b,1,2], Yue Zhao[c,1], Ryan T. VanderLinden[b,1], Wei Tuo[b], Fengmin Zhang[d], Shuwei Zhang[d], Hajar Sepehrpour[b], Chaoguo Yan[d], Jin Wang[d], Dan Li[d], and Peter J. Stang[b,2]

[a]State Key Laboratory Base of Novel Functional Materials and Preparation Science, School of Materials Science and Chemical Engineering, Ningbo University, Ningbo 315211, People's Republic of China; [b]Department of Chemistry, University of Utah, Salt Lake City, UT 84112; [c]Coordination Chemistry Institute, State Key Laboratory of Coordination Chemistry, School of Chemistry and Chemical Engineering, Nanjing National Laboratory of Microstructures, Collaborative Innovation Center of Advanced Microstructures, Nanjing University, Nanjing 210093, People's Republic of China; and [d]School of Chemistry and Chemical Engineering, Yangzhou University, Yangzhou 225002, People's Republic of China

Contributed by Peter J. Stang, May 7, 2021 (sent for review February 8, 2021; reviewed by Jean-Marie P. Lehn, Jeffrey S. Moore, and Vivian Wing-Wah Yam)

Polycyclic aromatic hydrocarbons (PAHs) continue to attract increasing interest with respect to their applications as luminescent materials. The ordered structure of the metal–organic complex facilitates the selective integration of PAHs that can be tuned to function cooperatively. Here, a unique highly twisted anthracene-based organoplatinum metallacycle was prepared via coordination-driven self-assembly. Single-crystal X-ray diffraction analysis revealed that the metallacycle was twisted through the cooperation of strong π···π stacking interactions and steric hindrance between two anthracene-based ligands. Notably, the intramolecular twist and aggregation behavior introduced restrictions to the conformational change of anthracenes, which resulted in increased emission intensity of the metallacycle in solution. The emission behaviors and suprastructures based on the highly twisted metallacycle can be modulated by the introduction of different solvents. This study demonstrates that this metallacycle with highly twisted structure is a promising candidate for sensing and bioimaging applications.

metal organic complex | highly twisted metallacycle | self-assembly

Weak intermolecular interactions play an essential role in the construction of well-defined hierarchical architectures with high complexity and functionality (1–4). In nature, a complex interplay of units forms highly organized suprastructures (5). From biofilms to cells, tissues, and organs, orderliness starts with the lipid bilayer and ultimately results in the formation of a macroscopically visible specific shape through multilevel assembly (6). Structurally, any macroscale organism maintains a high degree of orderliness on an extremely small scale, and this multilevel orderliness is carried through to the macroscale (7). DNA and histones coassemble to form chromatids, and chromatids further assemble to form chromosomes (8). Inspired by assemblies in the natural world, researchers have created diverse suprastructures with distinct spatial arrangements via weak interactions, such as hydrogen bonds, aromatic stacking, and hydrophobic interactions (9–19). Among these, coordination-driven self-assembly (CDSA) provides a powerful strategy for producing metal organic complexes (MOCs) with various sizes, shapes, and metal/ligand stoichiometries (20–26). To date, diverse MOCs have been developed by coordination between metal ions and organic ligands, and these exhibit superiority over their precursors and can be used in emission units, sensors, and hosts as well as in applications in biomedical diagnosis and catalysis (27–34). Platinum-based architectures are the most extensively studied of these structures and have undergone the most rapid development, due to their facile synthesis (35–39).

Platinum-based metallacycles are desirable candidates for the construction of luminophores because of their structural versatility. However, most luminophores always suffer from aggregation-induced quenching at high concentrations or in the solid state. Aggregation-induced emission has been employed in the fields of sensors, bioimaging, and drug delivery, due to strong emissions in the aggregated state (40, 41). However, to date, a tetraphenylethylene moiety is required in the construction of metallacycles with emission (42) Anthracene (ANTHR) is an attractive moiety that endows suprastructures with unique optical properties due to its extended π-surface (43, 44), which results in the formation of promising candidates for light emitters (45), photocatalysts (46), and data storage materials (47). For example, Zr and Fe have been incorporated with ANTHR into coordination complexes to perform catalysis (48) and to mimic the functional behavior of enzymes (49). In addition, ANTHR-based rectangles have been proven to provide near-infrared emission for application in ammonia detection (50), and ANTHR-based hexagons have been used for the capture and release of singlet oxygen (51). However, most reported ANTHR-based metallacycles have planar structures. Considering the relationship between structure and function of these metallacycles, the development of more structures with new steric features will lead to the emergence of new functions. This study provides

Significance

Macroscale organisms maintain a high degree of orderliness on an extremely small scale. Inspired by natural assemblies, anthracene-based organoplatinum metallacycles were designed as building blocks. Instead of the expected planar rectangles, a highly twisted structure was generated due to strong π···π stacking interactions and steric hindrance between the two anthracene ligands. Enhanced emission of the metallacycle in solution was observed due to restrictions on the conformational change of anthracenes introduced by the intramolecular twist and aggregation of metallacycle. The as-prepared twisted metallacycle was used as a building block to construct suprastructures. The optical properties and self-assembly behavior of the metallacycle in different solvent systems were systematically investigated. This study facilitates the rational design of metallacycle-based emissive multifunctional materials.

Author contributions: Y.S. and P.J.S. designed research; C.C., Y.S., R.T.V., and D.L. performed research; Y.S. contributed new reagents/analytic tools; C.C., Y.S., Y.Z., R.T.V., W.T., F.Z., S.Z., H.S., C.Y., J.W., and P.J.S. analyzed data; and C.C., Y.S., Y.Z., and P.J.S. wrote the paper.

Reviewers: J.-M.P.L., University of Strasbourg; J.S.M., University of Illinois at Urbana Champaign; and V.W.-W.Y., University of Hong Kong.

The authors declare no competing interest.

[1]C.C., Y.S., Y.Z., and R.T.V. contributed equally to this work.

[2]To whom correspondence may be addressed. Email: elaine.sun@utah.edu or stang@chem.utah.edu.

This article contains supporting information online at https://www.pnas.org/lookup/suppl/doi:10.1073/pnas.2102602118/-/DCSupplemental.

Published June 28, 2021.

an ANTHR-based metallacycle with a highly twisted conformation among ligands, and the twist angle between ANTHR is close to 90°. Benefiting from this highly twisted structure induced by intramolecular restriction, ANTHR-containing metallacycle with aggregation-induced emission was observed.

Results and Discussion

Here, ANTHR-based metallacycle was synthesized using ANTHR-based ligands (9,10-di(pyridin-4-yl)anthracene [DPA]), dicarboxylate moieties (isophthalic acid [IPA^{2-}]), and cis-$(PEt_3)_2Pt(OTf)_2$. The metallacycle was readily prepared using a heteroligation-directed three-component CDSA strategy. As shown in Scheme 1 *A* and *B*, metallacycle **1** was formed by the reaction of pyridyl-functionalized ANTHR ligand (**2**), dicarboxylate ligand (**3**), and phosphine-capped 90° Pt(II) acceptor (**4**) at a molar ratio of 1:1:2. Compounds **2** and **3** were dissolved in acetone and water, respectively. The two solutions were then mixed, and **4** in acetone was added. After heating at 60 °C for 12 h, the solvent was evaporated via N_2 flow. The resultant product **1** was obtained after drying under vacuum (*SI Appendix*). Metallacycle **1** was characterized by ^{1}H NMR (Scheme 1*C* and *SI Appendix*, Fig. S1) and $^{31}P\{^1H\}$ NMR (Scheme 1*D* and *SI Appendix*, Fig. S2) spectroscopy (52). As shown in the ^{1}H NMR spectrum of **1**, the protons of the pyridyl groups are located at δ = 8.68 and 7.14 ppm, which is attributed to the coordination of the N atoms to the platinum centers. The protons corresponding to dicarboxylate ligand **3** are observed at δ = 8.30, 8.09, and 7.46 ppm. The $^{31}P\{^1H\}$ spectrum also supported the structures. Further characterization by diffusion-ordered NMR spectroscopy (DOSY) was in agreement with the formation of discrete metallacycles (*SI Appendix*, Fig. S3). In the pseudo two-dimensional (2D) DOSY spectrum of **1**, all the proton signals from metallacycle are correlated with the same *D* of about $(10.0 \pm 0.4) \times 10^{-10}$ $m^2 \cdot s^{-1}$. Light green single crystals of the metallacycle were obtained by slow diffusion in dichloromethane (DCM) and ethyl acetate at room temperature. The ^{1}H NMR spectrum of **1** at variable temperature (VT NMR) in 1,2,-dichloroethane was determined to investigate the fluxionality of **1** (Fig. 1). As shown in Fig. 1 *A* and *B*, the H_{2a} and H_{2c} broadened with the temperature increase from 293 K to 323 K, and then coalesced to a single broad peak at 343 K. This might be caused by the faster rotation speed of the pyridinyl groups (H_{2a} and H_{2c}) at high temperature, resulting in the peaks becoming broader and even merging to one peak (the green regions on the left side in Fig. 1 *A* and *B*). At the same time, the peak of H_{2b} and H_{2d} also broadened with the temperature range from 293 K to 343 K (the green regions on the right side in Fig. 1 *A* and *B*), again caused by faster rotation at high temperature. The resonance of H_{3b} and H_{3c} maintained a

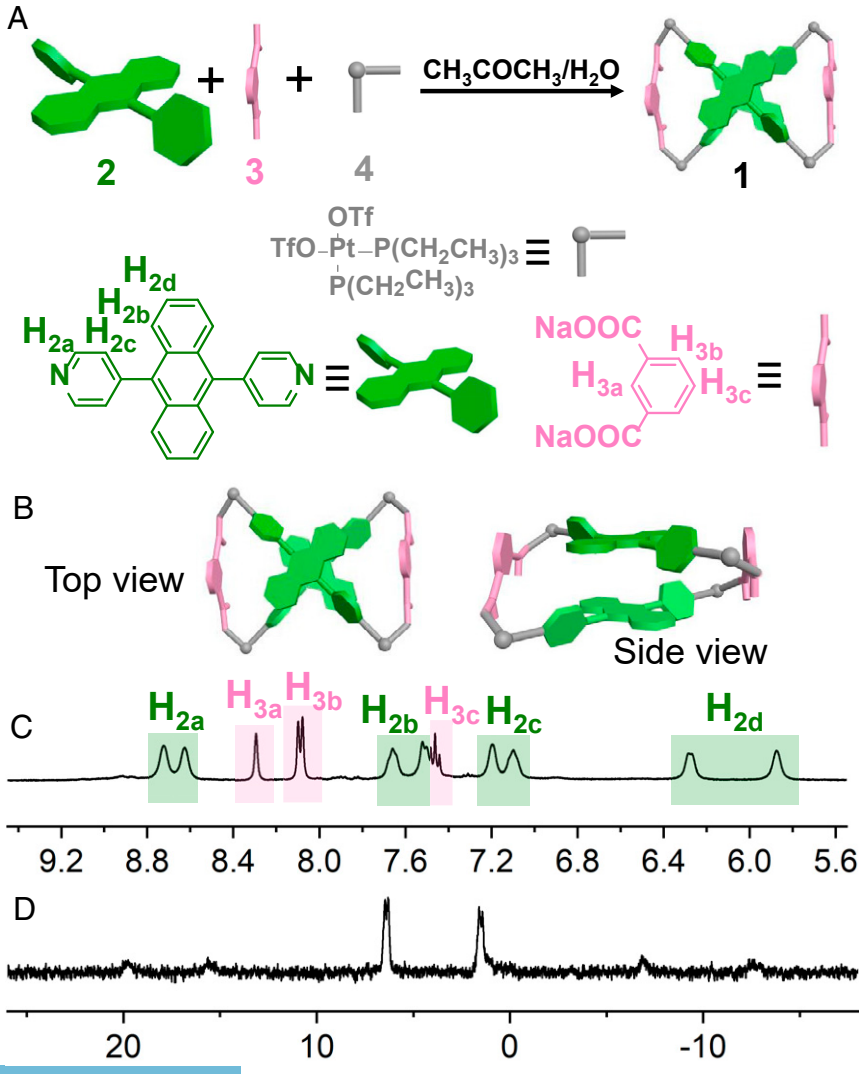

Scheme 1. (*A*) Chemical structure and self-assembly of metallacycle **1**. (*B*) Top and side views of **1**. (*C*) The ^{1}H NMR and (*D*) $^{31}P\{^1H\}$ NMR of **1**.

https://doi.org/10.1073/pnas.2102602118

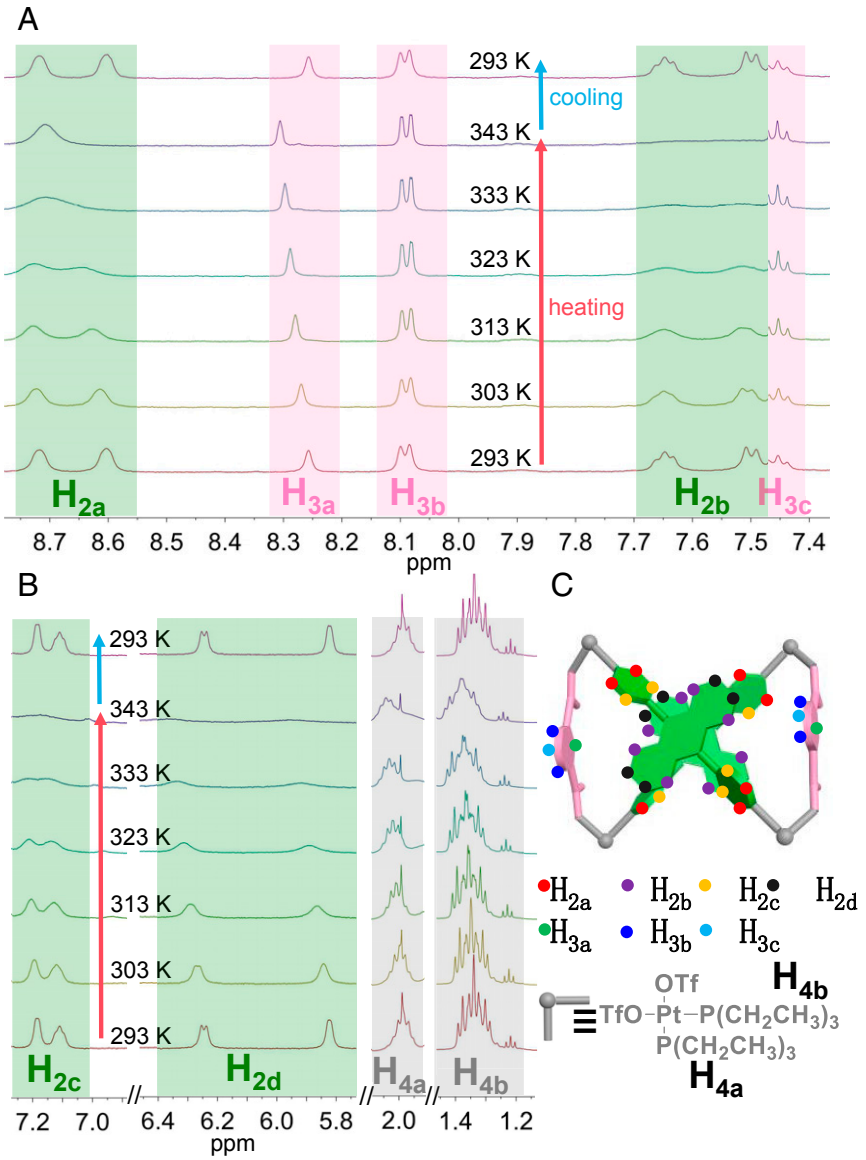

Fig. 1. (*A* and *B*) Variable-temperature NMR spectra of **1** in 1,2,-dichloroethane; (*C*) the scheme represents the proton of **1** in different chemical environment.

similar peak shape and intensity as the temperature increased, which proves the protons of the phenyl groups are less fluxional, due to the metasubstitution in the cycle. Different from the H_{3b} and H_{3c}, H_{3a} shows a downfield shift with the increase in temperature, which might be caused by the shortened distance between the protons and thus influenced by the ANTHR plane (pink region in Fig. 1 *A* and *B*). The environmental change of H_{4a} and H_{4b} can also be monitored by VT NMR, as shown in the gray region in Fig. 1*B*, and broader peaks can be observed with the increased temperature, which indicates a faster rotation speed of the σ-bonds. To make sure that these changes were reversible, the proton NMR was retaken after the temperature was cooled to 293 K. As shown in the top spectra in Fig. 1 *A* and *B*, all the peaks returned to the initial state at 293 K, indicating that no thermal reaction has taken place when heating from 293 K to 343 K, and no hysteresis is observed. Based on the above results, it is determined that the twist structure is fluxional in solution, especially in good solvents.

The structure of **1** was determined unambiguously by single-crystal X-ray diffraction, and the X-ray crystallographic analysis revealed the formation of a unique highly twisted metallacycle. As shown in Fig. 2*A*, the results from the X-ray diffraction analysis showed that the crystal structure of **1** contained a discrete organoplatinum(II) metallacycle, which consisted of two DPAs, two IPA^{2-}, four $(PEt_3)_2Pt(II)$ centers, and four triflate anions (OTf^-). In addition to the coordination bonds, variable noncovalent interactions, including π···π stacking interactions (4.282 Å), C–H···π interactions (2.839 Å) between the ANTHR moieties of DPA, C–H···π interactions (3.471 and 3.475 Å) between the hydrogen atoms on the ANTHR moieties of DPA and the benzene ring of IPA, and C–H···O hydrogen bonds between the hydrogen atoms on the ANTHR ring (C29–H29···O67, 2.516 Å) or the PEt_3 groups (C44A–H44B, 2.560 Å; C56A–H56C, 2.490 Å) and the carboxylate oxygen atoms of IPA^{2-}, facilitated the formation of the metallacycles (Fig. 2*B*). Despite the strong π···π and C–H···π stacking interactions between two ANTHR-based ligands, to minimize the steric effect between two ANTHR groups and enhance the π···π and C–H···π stacking interactions, the metallacycles adopted a twisted rectangular conformation with the ANTHR-based DPA ligands which was twisted by *ca*. 79.55° to form the metallacycle. Accordingly, the distance between the two ANTHR groups was compressed due to the twisted

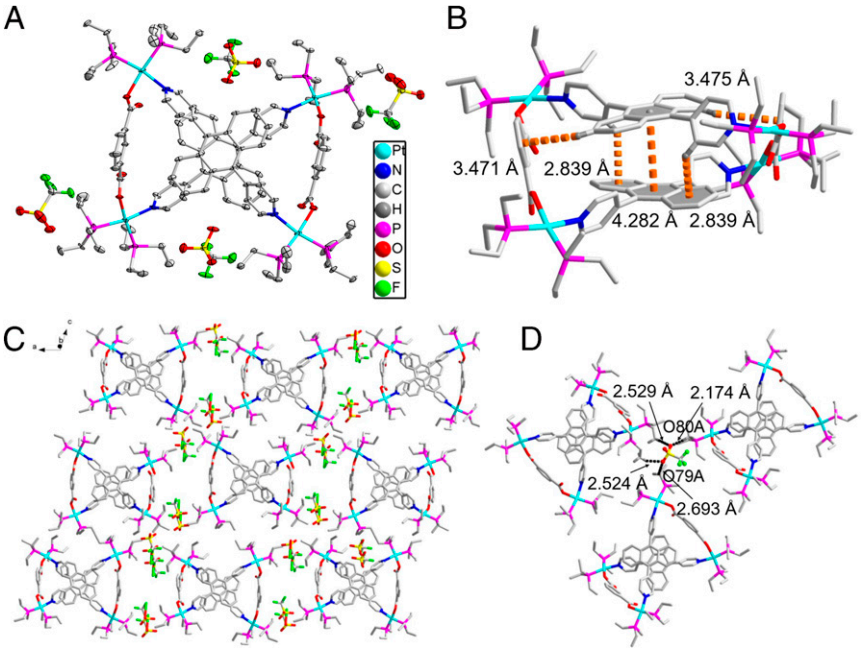

Fig. 2. (*A*) X-ray single-crystal structure of **1** with ellipsoids drawn at the 30% probability level. The hydrogen atoms are omitted for clarity. (*B*) Intramolecular π···π stacking interactions and C–H···π interactions in **1**. (*C*) The 2D network constructed from **1** linked by (*D*) intermolecular C–H···O hydrogen bonds.

structure. Furthermore, the crystallographically independent triflate anions were located in two different chemical environments and exhibited different multiple hydrogen-bonding modes.

The analysis of the crystallographically independent OTf^- anions (A) showed four intermolecular C–H···O hydrogen bonds with H···O distances of 2.174 Å to 2.693 Å (Fig. 2*D*). These hydrogen bonds assembled the adjacent metallacycles into 2D infinite supramolecular networks (Fig. 2*C*). For the OTf^- anion (B), four C–H···O hydrogen bonds ($d_{H\cdots O}$: 2.395 Å to 2.687 Å; Fig. 3*A*) and two C–H···F hydrogen bonds ($d_{H\cdots F}$: 2.568 and 2.600 Å; Fig. 3*A*) formed between the two metallacycles from two adjacent 2D networks and joined the 2D networks to form the final 3D supramolecular architecture with large rectangular channels running along the b axis (*SI Appendix*, Fig. S4). In addition, multiple π···π stacking interactions (4.337 Å) and C–H···π interactions (2.841 Å to 2.898 Å) were observed between the ANTHR moieties of DPA from the metallacycles in the neighboring 2D networks, and these interactions helped stabilize the final 3D supramolecular structure of **1** (Fig. 2*B*). Due to the C–H···π interactions between the pyridine rings and the ANTHR moieties on the ligand DPA, the pyridine rings were rotated up to 55.87° and 60.30° with respect to the central ANTHR plane (Fig. 3*C*).

To reveal the optical properties of the twisted structure, the absorption and emission spectra of both precursor **2** and metallacycle **1** in DCM, acetone, and ethanol were monitored. Both the absorption and emission spectra were normalized for wavelength

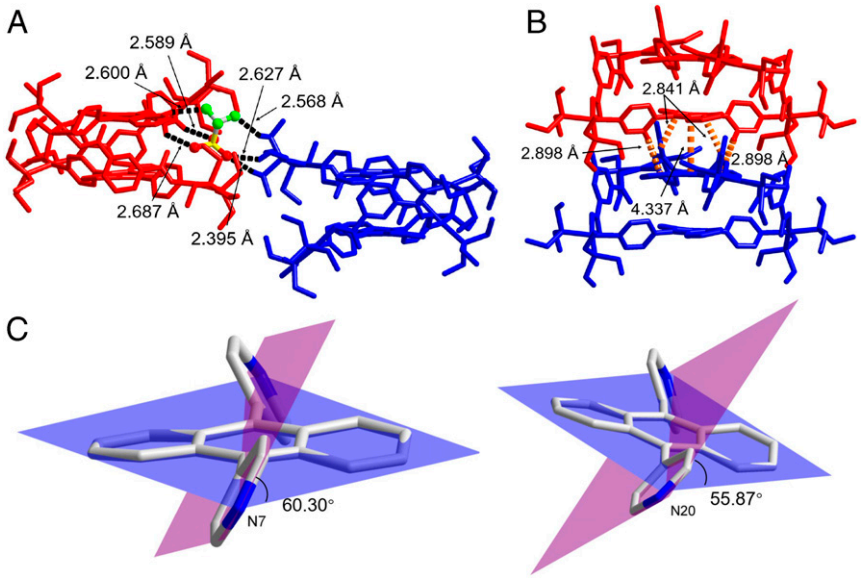

Fig. 3. (*A*) Hydrogen bonds between the metallacycles and OTf^- anions. (*B*) π···π stacking interactions and C–H···π interactions between adjacent metallacycles. (*C*) Dihedral angles between the pyridine rings and ANTHR moieties.

shift comparison. As shown in the ultraviolet–visible (UV–Vis) spectra in Fig. 4*A*, in acetone (green dashed line), the absorption peaks at 353 nm (0–2 transition), 372 nm (0–1 transition) and 392 nm (0–0 transition); in ethanol (blue dashed line), the absorption peaks at 353 nm (0–2 transition), 372 nm (0–1 transition) and 391 nm (0–0 transition). However, different from the absorption in acetone and in ethanol, only a broad band with a peak at 404 nm was observed in DCM (orange dashed line). To be sure of the origin of the absorption change in DCM, the absorption of precursor **2** in the three solvents was also recorded. As shown in the UV–Vis spectra in *SI Appendix*, Fig. S6*A*, almost identical absorption peaks at 352, 370, and 390 nm were recorded in acetone and ethanol. In DCM, the peaks slightly redshift to 353, 371, and 392 nm. Nevertheless, they had similar absorption bands. Therefore, the unusual broad absorptions of **1** in DCM most likely originate from the twist structure and resultant fast rotation in good solvents. The emission spectra of **1** and the precursor **2** in different solvents are shown in Fig. 4*A* and *SI Appendix*, Fig. S6*B*. It should be noted that the emission of **1** is located at 434 nm, with a small shoulder peak (410 nm) in acetone (green solid line in Fig. 4*A*). Different from the spectra in acetone, **1** in ethanol (blue solid line) and DCM (orange solid line) shows only two emission peaks at 447 and 466 nm, respectively (Fig. 4*A*). These observed emission bands in the region with wavelengths of <500 nm are due to a spin-allowed transition, and the emissions are thus due to fluorescence (53, 54). The VT NMR data reveal the fluxionality of the ANTHR in DCM, therefore the different spectra might be caused by the different solubility of **1** in different solvents, which limits the twist of the ANTHR in a specific solvent.

This solubility-caused spectral change is further demonstrated by the absorption and emission spectra in DCM/ethyl acetate (EA) with a change in EA ratio (Fig. 4*B*). For **1** in pure DCM, the maximum absorption peak is located at 404 nm. At an EA ratio of 20%, the 404-nm absorption is blue shifted to 395 nm. When the EA ratio is 40%, two new peaks at 375 and 355 nm appear. Moreover, the absorption at 391 nm (0–0 transition) continues to increase. With the EA content increased to 60%, all the peak intensities at 391 nm (0–0 transition), 375 nm (0–1 transition), and 355 nm (0–2 transition) increase (*SI Appendix*, Fig. S8). The reason for the change of absorption bands and increasing emission intensity is that the addition of EA induces the aggregation of **1** in solution and thus introduces further restrictions to the conformational change of the metallacycle and decreases the fluxionality of **1** in solution (42). Similar wavelength blueshift was also observed in the fluorescence spectra. The emission blue shifted from 466 nm (pure DCM) to 464 nm (20% EA), then to 461 nm (40% EA), and to 459 nm (60% EA). Moreover, a new peak at 409 nm appears, and the intensity increases when the EA content increases (Fig. 4*B*). As shown in Fig. 4*C*, the Commission Internationale de l'Éclairage (CIE) diagram shows the color of **1** in DCM and the gradual blueshift with decreases in the DCM content (Fig. 4*D*). The CIE analysis shows emission colors of (0.129, 0.262) in pure DCM, and the color changes from (0131, 0.239) to (0.135, 0.197) to (0.139, 0.155) as the EA content increases (from 20% to 40%, then to 60%).

To investigate the optical properties systematically, the absorption and emission spectra of **1** in acetone/water mixtures were studied (*SI Appendix*, Fig. S9). As shown in *SI Appendix*, Fig. S9*A*, the absorption spectra of **1** in acetone exhibited three peaks, 353, 372, and 392 nm, and remain unchanged as the water content is increased from 0 to 40%. The disappearance of the shoulder peak was observed in the analysis of the emission spectra in acetone/water. As the water content is changed from 0 to 40%, the two emission peaks at 410 and 434 nm in pure acetone merge into a new peak at 425 nm in a 40% acetone/water mixture (*SI Appendix*, Fig. S9*A*). As the water content is changed from 0 to 40%, an obvious increase in the intensity of the emission was observed, due to the aggregation of **1** (*SI Appendix*, Fig. S9*B*). The CIE analysis of **1** in acetone/water shows a change in the emission color from (0.148, 0.074) to (0.155, 0.037) as the water content increases (*SI Appendix*, Fig. S10).

Subsequently, the aggregation behavior of **1** was investigated by transmission electron microscopy (TEM) and scanning TEM (STEM). **1**-based assemblies were obtained by the assembly of **1** in DCM/EA. The overall STEM images of the **1**-based assemblies in a DCM/EA mixture are shown in *SI Appendix*, Fig. S11. The images indicate that nanospheres of ∼100 nm were formed. Energy-dispersive X-ray (EDX) mapping analysis confirmed the homogeneous distributions of N, Pt, P, F, S, and O across the spheres and provided evidence showing that the spheres were composed of ANTHR, cis-Pt-$(PEt_3)_2(OTf)_2$, and carboxylate ligands (Fig. 4*E*). These results prove the formation of nanospheres by the assembly of ANTHR-based platinum metallacycles. The observation of aggregates further suggested that the twisted cycle and its higher clusters in solution led to fluorescent enhancement. STEM observations obtained after EA was changed to another solvent, n-pentane, revealed the formation of cluster-like assemblies in the DCM/n-pentane mixture with 80% n-pentane (Fig. 5 *A* and *B*). The distributions of N, Pt, P, F, S, and O in the assemblies were verified by EDX mapping analysis (Fig. 5*C*), and the results confirmed that the assemblies were composed of metallacycle **1**. The magnification of the assemblies indicated a cluster with uniform size (Fig. 5*D* and *SI Appendix*, Fig. S12), and the histograms of the size distribution of these clusters are illustrated in Fig. 5*E*. As revealed by the histograms, the average diameter and SD were 0.88 ± 0.16 μm. Furthermore, a sheet-based intermediate was observed (Fig. 5*F*), which demonstrated that sheets were the origin of the resultant clusters. For further investigations, highly polar protic solvent water was added to acetone to induce the self-assembly of **1**. The self-assembly behavior of **1** in acetone/water mixtures was studied by TEM, which revealed the formation of irregular ANTHR-based assemblies in acetone/water with 80% water (*SI Appendix*, Fig. S13).

Then, to get further insight into the self-assembly behaviors of **1**, dynamic light scattering (DLS) was used to monitor the aggregate size. Given that the size of **1** calculated from the crystal structure is *ca.* 1.5 nm (*SI Appendix*, Fig. S14 *A* and *B*), the DLS results indicate that most of the metallacycles assemble into large aggregates in solution. For metallacycle **1** in the DCM/EA system, the average hydrodynamic diameter of aggregates increased from 51 nm to 218 nm with an increasing fraction of EA from 20 to 80% (*SI Appendix*, Fig. S14*C*), demonstrating that the size of the nanospheres increased when the EA content increased. In addition, the size observed is in good agreement with the aggregates in Fig. 4*E*. Similar results were observed in DCM/n-pentane mixtures. The increasing n-pentane fraction induces the formation of larger self-assembly, with a mean size of 274 nm (*SI Appendix*, Fig. S14*D*). This is in accordance with the TEM observation that the cluster-like assemblies originate from sheet-based intermediates. In acetone/water mixture with 20% water, bimodal signals were detected with mean sizes of 85 and 319 nm (*SI Appendix*, Fig. S14*E*). Upon the addition of water, the smaller aggregates further assembled to form the larger aggregates, and the bimodal peak fused to form a unimodal one.

As mentioned above, this metallacycle with a twisted structure shows both tunable emissions and self-assembly behaviors. Considering the highly twisted structure revealed in this study, in the future, by overcoming the strong π···π stacking interactions between ANTHR groups, we will focus on the design of ligands that can induce inversion of the twist, making them a unique candidate for sensing and bioimaging applications.

Conclusion

This study reveals the importance of the interaction between rigid aromatic moieties in the formation of highly organized supramolecular structures. In addition, it provides a strategy for the fabrication of ANTHR-containing highly twisted emissive metallacycle stabilized by π···π stacking interactions. Meanwhile, the fluorescence emission and aggregate morphology of the resultant metallacycle can

CHEMISTRY

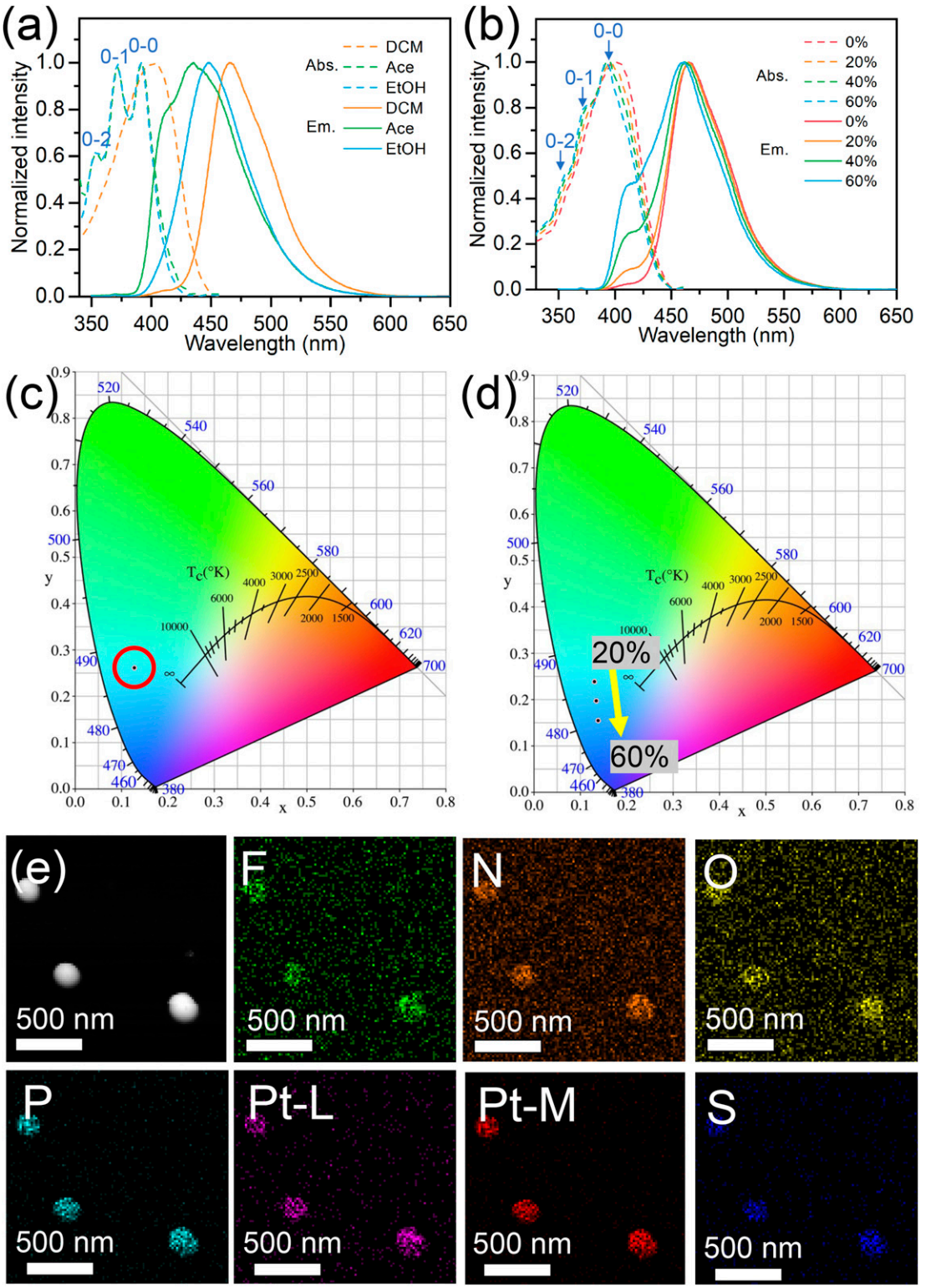

Fig. 4. (*A*) Normalized UV absorption spectra and fluorescence emission spectra of **1** (10 μM) in different solvents. (*B*) Normalized UV absorption spectra and fluorescence emission spectra of **1** (10 μM) in DCM/EA mixtures with different fractions of EA. (*C* and *D*) CIE diagram of **1** in (*C*) DCM and (*D*) DCM/EA mixtures with different fractions of EA. (*E*) STEM image and EDX mapping images of **1**-based self-assemblies in a DCM/EA mixture (80% EA).

be systematically tuned by changing the binary solvent systems. As mentioned above, this work will open up avenues for developing emissive ANTH-based multifunctional materials via weak intermolecular interactions.

Materials and Methods

All reagents were commercially available and used as supplied without further purification. Deuterated solvents were purchased from Cambridge Isotope Laboratory. Compounds **2**, **3**, and **4** were prepared according to modified

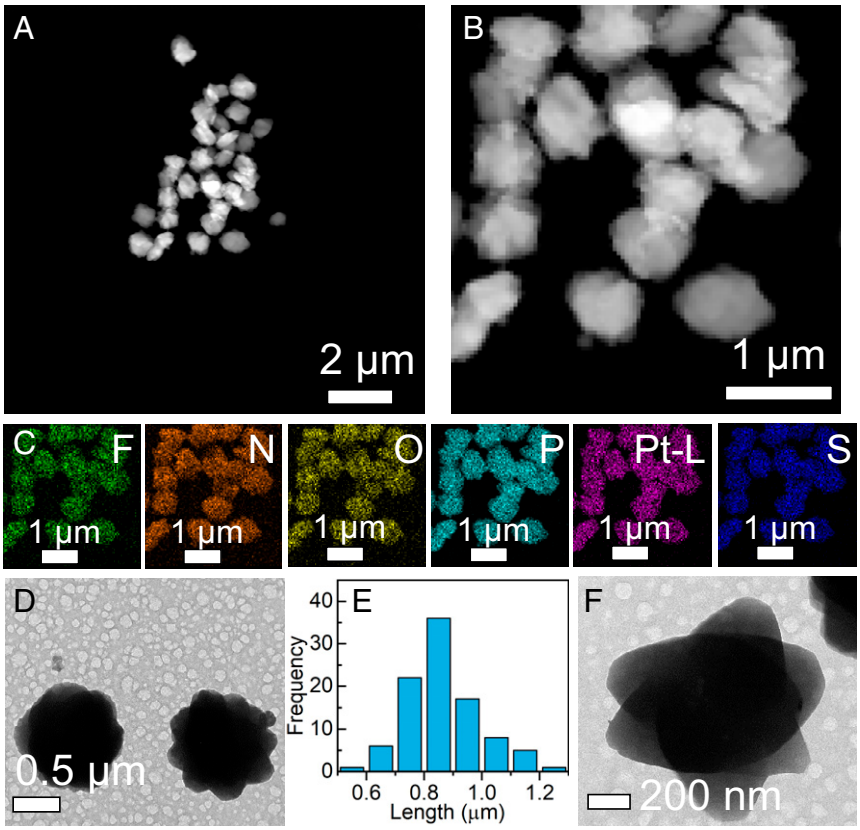

Fig. 5. (*A* and *B*) STEM images, (*C*) corresponding element distribution, (*D* and *F*) magnification of TEM images, and (*E*) histogram of the size distribution of **1**-based self-assemblies in a DCM/n-pentane mixture (80% n-pentane).

procedures detailed in the literature. NMR spectra were recorded using a spectrometer at room temperature, and ^{1}H NMR spectra were recorded in the designated solvents using a Varian Inova 400-MHz spectrometer. The DOSY NMR spectra and variable-temperature NMR spectra were recorded on a Varian Inova 500-MHz spectrometer. The $^{31}P\{^{1}H\}$ NMR spectra were obtained using on a Varian Unity 300 NMR spectrometer, and the $^{31}P\{^{1}H\}$ NMR chemical shifts were referenced to an external unlocked sample of 85% H_3PO_4 (δ 0.0 ppm). To minimize the interpretation of solid particulates to the optical characterization, the data measured from turbid solutions were not recorded. The TEM investigations were performed with a JEM-2100EX instrument. For TEM, dispersions of the assemblies were dried on carbon-coated copper support grids. High resolution TEM images were obtained using a Tecnai G2 F30 S-TWIN instrument. A Zeiss Supra55 field-emission scanning electron microscope was used to investigate the assemblies. For SEM, dispersions of the assemblies were dried on silicon wafers. Size distribution was measured by a ZetaPALS analyzer (Brookhaven).

Data Availability. All study data are included in the article and *SI Appendix*.

ACKNOWLEDGMENTS. Y.S. and P.J.S. thank Peter Flynn and Dennis Edwards for DOSY and VT-NMR discussion.

1. W. Jiang *et al*., Emergence of complexity in hierarchically organized chiral particles. *Science* **368**, 642–648 (2020).
2. Y. Sun *et al*., Self-assembly of metallacages into centimeter films with tunable size and emissions. *J. Am. Chem. Soc.* **142**, 17933–17937 (2020).
3. Z. Yang, J.-M. Lehn, Dynamic covalent self-sorting and kinetic switching processes in two cyclic orders: Macrocycles and macrobicyclic cages. *J. Am. Chem. Soc.* **142**, 15137–15145 (2020).
4. X. Jiang *et al*., Kinetic control in the synthesis of a Möbius tris((ethynyl)[5]helicene) macrocycle using alkyne metathesis. *J. Am. Chem. Soc.* **142**, 6493–6498 (2020).
5. N. Reznikov, M. Bilton, L. Lari, M. M. Stevens, R. Kröger, Fractal-like hierarchical organization of bone begins at the nanoscale. *Science* **360**, eaao2189 (2018).
6. V. Chaikeeratisak *et al*., Assembly of a nucleus-like structure during viral replication in bacteria. *Science* **355**, 194–197 (2017).
7. R. M. Capito, H. S. Azevedo, Y. S. Velichko, A. Mata, S. I. Stupp, Self-assembly of large and small molecules into hierarchically ordered sacs and membranes. *Science* **319**, 1812–1816 (2008).
8. Z. Holubcová, M. Blayney, K. Elder, M. Schuh, Human oocytes. Error-prone chromosome-mediated spindle assembly favors chromosome segregation defects in human oocytes. *Science* **348**, 1143–1147 (2015).
9. Y. Yao *et al*., A pillar[5]arene based gel from a low-molecular-weight gelator for sustained dye release in water. *Dalton Trans.* **46**, 16802–16806 (2017).
10. Y. Sun, W. Fu, Z. Li, Z. Wang, Tailorable aqueous dispersion of single-walled carbon nanotubes using tetrachloroperylene-based bolaamphiphiles via noncovalent modification. *Langmuir* **30**, 8615–8620 (2014).
11. M. Shen, W.-f. Chen, Y. Sun, C.-g. Yan, Synthesis and characterization of water-soluble gold colloids stabilized with aminoresorcinarene. *J. Phys. Chem. Solids* **68**, 2252–2261 (2007).
12. L. Li *et al*., Resorcinarene induced assembly of carotene and lutein into hierarchical superstructures. *J. Am. Chem. Soc.* **142**, 20583–20587 (2020).
13. Y. Sun, Z. Li, In situ polymerization of supramolecular nanorods assembled from polymerizable perylene bisimide. *Polym. Chem.* **8**, 4422–4427 (2017).
14. H. Zhu *et al*., Formation of planar chiral platinum triangles via pillar[5]arene for circularly polarized luminescence. *J. Am. Chem. Soc.* **142**, 17340–17345 (2020).
15. F. Guo, Y. Sun, B. Xi, G. Diao, Recent progress in the research on the host-guest chemistry of pillar[n]arenes. *Supramol. Chem.* **30**, 81–92 (2018).
16. J. Sun *et al*., Electrochemical detection of paraquat based on silver nanoparticles/water-soluble pillar 5 arene functionalized graphene oxide modified glassy carbon electrode. *J. Electroanal. Chem.* **847**, 113221 (2019).
17. J. Lee *et al*., Expanding the limits of the second genetic code with ribozymes. *Nat. Commun.* **10**, 5097 (2019).
18. M.-Y. Leung *et al*., Multiresponsive luminescent cationic cyclometalated gold(III) amphiphiles and their supramolecular assembly. *J. Am. Chem. Soc.* **141**, 19466–19478 (2019).
19. E. Raee, Y. Yang, T. Liu, Supramolecular structures based on metal-organic cages. *Giant* **5**, 100050 (2021).
20. H. Takezawa, K. Shitozawa, M. Fujita, Enhanced reactivity of twisted amides inside a molecular cage. *Nat. Chem.* **12**, 574–578 (2020).
21. D. A. Roberts, B. S. Pilgrim, J. R. Nitschke, Covalent post-assembly modification in metallosupramolecular chemistry. *Chem. Soc. Rev.* **47**, 626–644 (2018).
22. X. Yan *et al*., Supramolecular polymers with tunable topologies via hierarchical coordination-driven self-assembly and hydrogen bonding interfaces. *Proc. Natl. Acad. Sci. U.S.A.* **110**, 15585–15590 (2013).

23. H. Wang, Y. Li, N. Li, A. Filosa, X. Li, Increasing the size and complexity of discrete 2D metallosupramolecules. *Nat. Rev. Mater.* **6**, 145–167 (2020).
24. Z. Yang *et al.*, Hierarchical self-assembly of a pyrene-based discrete organoplatinum(II) double-metallacycle with triflate anions via hydrogen bonding and its tunable fluorescence emission. *J. Am. Chem. Soc.* **142**, 13689–13694 (2020).
25. T. Hong *et al.*, Chiral metallacycles as catalysts for asymmetric conjugate addition of styrylboronic acids to α,β-enones. *J. Am. Chem. Soc.* **142**, 10244–10249 (2020).
26. J. K.-L. Poon, Z. Chen, S. Y.-L. Leung, M.-Y. Leung, V. W.-W. Yam, Geometrical manipulation of complex supramolecular tessellations by hierarchical assembly of amphiphilic platinum(II) complexes. *Proc. Natl. Acad. Sci. U.S.A.* **118**, e2022829118 (2021).
27. Y. Sun, C. Chen, J. Liu, P. J. Stang, Recent developments in the construction and applications of platinum-based metallacycles and metallacages via coordination. *Chem. Soc. Rev.* **49**, 3889–3919 (2020).
28. Y. Sun, C. Chen, P. J. Stang, Soft materials with diverse suprastructures via the self-assembly of metal-organic complexes. *Acc. Chem. Res.* **52**, 802–817 (2019).
29. H. Sepehrpour, W. Fu, Y. Sun, P. J. Stang, Biomedically relevant self-assembled metallacycles and metallacages. *J. Am. Chem. Soc.* **141**, 14005–14020 (2019).
30. W. Chen *et al.*, β-Cyclodextrin modified Pt(II) metallacycle-based supramolecular hyperbranched polymer assemblies for DOX delivery to liver cancer cells. *Proc. Natl. Acad. Sci. U.S.A.* **117**, 30942–30948 (2020).
31. Y. Sun *et al.*, Melanin-dot-mediated delivery of metallacycle for NIR-II/photoacoustic dual-modal imaging-guided chemo-photothermal synergistic therapy. *Proc. Natl. Acad. Sci. U.S.A.* **116**, 16729–16735 (2019).
32. Y. Sun *et al.*, Rhomboidal Pt(II) metallacycle-based NIR-II theranostic nanoprobe for tumor diagnosis and image-guided therapy. *Proc. Natl. Acad. Sci. U.S.A.* **116**, 1968–1973 (2019).
33. G. Yu *et al.*, Host-guest complexation-mediated codelivery of anticancer drug and photosensitizer for cancer photochemotherapy. *Proc. Natl. Acad. Sci. U.S.A.* **116**, 6618–6623 (2019).
34. Y. Zhao *et al.*, Self-assembled ruthenium (II) metallacycles and metallacages with imidazole-based ligands and their in vitro anticancer activity. *Proc. Natl. Acad. Sci. U.S.A.* **116**, 4090–4098 (2019).
35. Y. Sun *et al.*, Self-assembly of porphyrin-based metallacages into octahedra. *J. Am. Chem. Soc.* **142**, 17903–17907 (2020).
36. X. Jiang *et al.*, Self-assembly of porphyrin-containing metalla-assemblies and cancer photodynamic therapy. *Inorg. Chem.* **59**, 7380–7388 (2020).
37. Y. Sun *et al.*, Assembly of metallacages into soft suprastructures with dimensions of up to micrometers and the formation of composite materials. *J. Am. Chem. Soc.* **140**, 17297–17307 (2018).
38. Y. Sun *et al.*, Self-assembly of metallacages into multidimensional suprastructures with tunable emissions. *J. Am. Chem. Soc.* **140**, 12819–12828 (2018).
39. M. Zhang *et al.*, Metallacycle-cored supramolecular assemblies with tunable fluorescence including white-light emission. *Proc. Natl. Acad. Sci. U.S.A.* **114**, 3044–3049 (2017).
40. J. Li *et al.*, Supramolecular materials based on AIE luminogens (AIEgens): Construction and applications. *Chem. Soc. Rev.* **49**, 1144–1172 (2020).
41. F. Würthner, Aggregation-induced emission (AIE): A historical perspective. *Angew. Chem. Int. Ed. Engl.* **59**, 14192–14196 (2020).
42. X. Yan, T. R. Cook, P. Wang, F. Huang, P. J. Stang, Highly emissive platinum(II) metallacages. *Nat. Chem.* **7**, 342–348 (2015).
43. N. Das, A. Ghosh, A. M. Arif, P. J. Stang, Self-assembly of neutral platinum-based supramolecular ensembles incorporating oxocarbon dianions and oxalate. *Inorg. Chem.* **44**, 7130–7137 (2005).
44. N. Das, P. J. Stang, A. M. Arif, C. F. Campana, Synthesis and structural characterization of carborane-containing neutral, self-assembled Pt-metallacycles. *J. Org. Chem.* **70**, 10440–10446 (2005).
45. S. Haldar *et al.*, Anthracene-resorcinol derived covalent organic framework as flexible white light emitter. *J. Am. Chem. Soc.* **140**, 13367–13374 (2018).
46. T. Uchikura, M. Oshima, M. Kawasaki, K. Takahashi, N. Iwasawa, Supramolecular photocatalysis by utilizing the host-guest charge-transfer interaction: Visible-light-induced generation of triplet anthracenes for [4+2] cycloaddition reactions. *Angew. Chem. Int. Ed. Engl.* **59**, 7403–7408 (2020).
47. M. Tu *et al.*, Reversible optical writing and data storage in an anthracene-loaded metal-organic framework. *Angew. Chem. Int. Ed. Engl.* **58**, 2423–2427 (2019).
48. C. H. Low, J. N. Rosenberg, M. A. Lopez, T. Agapie, Oxidative coupling with Zr(IV) supported by a noninnocent anthracene-based ligand: Application to the catalytic cotrimerization of alkynes and nitriles to pyrimidines. *J. Am. Chem. Soc.* **140**, 11906–11910 (2018).
49. S. A. Kerns, A.-C. Magtaan, P. R. Vong, M. J. Rose, Functional hydride transfer by a thiolate-containing model of mono-iron hydrogenase featuring an anthracene scaffold. *Angew. Chem. Int. Ed. Engl.* **57**, 2855–2858 (2018).
50. Z. Li, X. Yan, F. Huang, H. Sepehrpour, P. J. Stang, Near-infrared emissive discrete platinum(II) metallacycles: Synthesis and application in ammonia detection. *Org. Lett.* **19**, 5728–5731 (2017).
51. Y.-Q. He *et al.*, Capture and release of singlet oxygen in coordination-driven self-assembled organoplatinum(II) metallacycles. *J. Am. Chem. Soc.* **142**, 2601–2608 (2020).
52. Y. Shi, I. Sánchez-Molina, C. Cao, T. R. Cook, P. J. Stang, Synthesis and photophysical studies of self-assembled multicomponent supramolecular coordination prisms bearing porphyrin faces. *Proc. Natl. Acad. Sci. U.S.A.* **111**, 9390–9395 (2014).
53. M. A. Omary, H. H. Patterson, "Luminescence, theory" in *Encyclopedia of Spectroscopy and Spectrometry*, J. C. Lindon, G. E. Tranter, D. W. Koppenaal, Eds. (Academic, ed. 3, 2017), pp. 636–653.
54. Y. Sun, P. J. Stang, Metallacycles, metallacages and their aggregate/optical Behavior. *Aggregate*, 10.1002/agt2.94 (2021) in press.